

Infrared Techniques for Measuring Ocean Surface Processes

FABRICE VERON

College of Marine and Earth Studies, University of Delaware, Newark, Delaware

W. KENDALL MELVILLE AND LUC LENAIN

Scripps Institution of Oceanography, University of California, San Diego, La Jolla, California

(Manuscript received 21 August 2006, in final form 21 February 2007)

ABSTRACT

Ocean surface processes, and air–sea interaction in general, have recently received increased attention because it is now accepted that small-scale surface phenomena can play a crucial role in the air–sea fluxes of heat, mass, and momentum, with important implications for weather and climate studies. Yet, despite good progress in recent years, the air–sea interface and the adjacent atmospheric and marine boundary layers have proven to be difficult to measure in all but the most benign conditions. This has led to the need for novel measurement techniques to quantify processes of air–sea interaction. Here the authors present infrared techniques aimed at simultaneously studying multiple aspects of the air–sea interface and air–sea fluxes. The instrumentation was tested and deployed during several field experiments from Research Platform (R/P) *FLIP* and Scripps pier. It is shown that these techniques permit the detailed study of the ocean surface temperature and velocity fields. In particular, it is shown that cross-correlation techniques typically used in particle image velocimetry can be used to infer the ocean surface velocity field from passive infrared temperature images. In addition, when conditions make cross-correlation techniques less effective, an active infrared marking and tracking technique [which will be called thermal marker velocimetry (TMV)] can be successfully used to measure the surface velocity and its spatial and temporal derivatives. The thermal marker velocimetry technique also provides estimates of the heat transfer velocity and surface renewal frequencies. Finally, infrared altimetry is used to complement the temperature and kinematic data obtained from passive imagery and active marking. The data obtained during the testing and deployment of this instrumentation provide a novel description of the kinematics of the surface of the ocean.

1. Introduction

Ocean surface processes control the air–sea fluxes of heat, mass, and momentum, and consequently play a crucial role in the evolution of weather and global climate. Exchanges between the atmosphere and the ocean must necessarily transfer through the surface and the rates at which they do is greatly influenced by the dynamics. This is particularly true for the transfer of heat and mass (gas) through the molecular, diffusive sublayer at the ocean surface. The momentum too is transferred through the surface viscous sublayer, but there is also a component of the stress that is carried by the waves and balanced by the wave growth. As a re-

sult, attention has recently been focused on the small-scale processes that influence the dynamics of the surface, and consequently, much progress has been made to quantify these air–sea transfers for a wide range of wind and wave conditions. It has been found that small-scale processes such as (breaking) waves, turbulence on both sides of the interface, bubbles, and droplets may play an important role in these fluxes. For example, it was found that breaking waves (Agrawal et al. 1992; Thorpe 1993; Melville 1994; Anis and Moum 1995; Melville 1996; Terray et al. 1996; Veron and Melville 1999a), along with small-scale Langmuir circulations and coherent structures (Melville et al. 1998; Veron and Melville 1999b, 2001), may lead to enhanced levels of turbulence and mixing, and heat and gas transfer (Jähne et al. 1987; Hasse 1990; Jähne and Haußecker 1998; Zappa et al. 2001; Garbe et al. 2004; Schimpf et al. 2004; Turney et al. 2005). Despite the fact that global heat budgets are now at the forefront of

Corresponding author address: Fabrice Veron, 112C Robinson Hall, University of Delaware, College of Marine and Earth Studies, Newark, DE 19716.
E-mail: fveron@udel.edu

current research in atmospheric, oceanographic, and climate sciences, and despite the good progress in recent years, much remains to be done to better understand and quantify air–sea exchanges.

While attention has historically focused on larger-scale longer-term phenomena, the mechanisms involved in small-scale mixing still remain rather poorly understood. In fact, very little is known about their intermittent nature, which may very well dominate the long-term behavior of the upper layers of the ocean, especially at low wind speeds. In addition, with the difference between kinematic viscosity and thermal diffusivity being almost one order of magnitude, the thermal sublayer is typically within the viscous sublayer. This points to the need for high temporal and spatial measurements that integrate both surface thermal and kinematic properties of the surface. Infrared thermal imaging techniques therefore appear promising in this regard.

In recent decades, radiometric and infrared techniques have been used to remotely sense sea surface temperature (SST), a key parameter in air–sea interaction and an important component of models of air–sea heat and moisture transfers (Soloviev and Schlüssel 1994; Fairall et al. 1996). Early infrared measurements were geared toward the investigation of the thermal boundary layer at the ocean surface and how it relates to the oceanic heat flux (Ewing and McAlister 1960; McAlister 1964; Saunders 1967; McAlister and McLeish 1970; Hill 1972). Later, measurements of the so-called cool skin were made in the context of remote and satellite sea surface temperature measurements. Indeed, since the net heat flux from the ocean to the atmosphere is generally positive upward, the surface temperature, or skin temperature, is typically a few tenths of a degree colder than the bulk sea temperature. This leads to what is now referred to as the “cool skin” bias in remote sea surface temperature measurements, which thereby prevents bulk sea surface temperature measurements from being made with high accuracy using radiometric data (Saunders 1967; Schlüssel et al. 1990; Donlon and Robinson 1997; Castro et al. 2003). Much effort has been spent on trying to quantify this bias to correct remote SST measurements (Wick et al. 1992; Fairall et al. 1996; Wick et al. 1996). Recently, infrared measurements of the sea surface have been used to detect breaking waves (Jessup et al. 1997b), microscale breaking waves (Jessup et al. 1997a; Zappa et al. 2001), fronts and internal wave structures (Zappa and Jessup 2005), and also used to infer gas flux (Jähne and Haußecker 1998; Garbe et al. 2004; Asher et al. 2004).

In this paper, we present an integrated infrared imaging and altimetry system designed to use nonintru-

sive, active, and passive infrared techniques to study multiple processes at the ocean surface.

2. Instrumentation and deployment

a. Instrumentation

The instrumentation described here is part of an integrated field-deployable optical and infrared imaging and altimetry system. It includes an infrared digital camera (Amber Galileo), a 60-W air-cooled CO₂ laser (Synrad Firestar T60) equipped with an industrial marking head (Synrad FH index) with two computer-controlled scanning mirrors, a laser altimeter (Riegl LD90–3100-EHS), a video camera (Pulnix TM-9701), a 6 degree-of-freedom motion package (Watson Gyro), and a single board computer (PC Pentium 4). Figure 1 shows photographs of the equipment layout. The side view shows the instruments mounted on a 3/4-inch-thick aluminum plate, prior to installation inside the weatherproof air-conditioned aluminum housing. The top side view shows the instruments inside the lower part of the housing. The layout of the imaging instruments was designed with the altimeter footprint (approximately 5 cm in diameter) within the footprint of the infrared image, which in turn is within the footprint of the video images. The lower part of the housing was fitted with view ports sealed with optical-grade windows for each optical instrument. The CO₂ laser viewport was sealed with a 6.4-cm-diameter Germanium window coated for 10.6- μm wavelength. The infrared camera viewport was equipped with a 6.4-cm-diameter Germanium window coated for 3–5- μm radiation, which is the range of wavelengths at which the infrared imager operates. All the viewports were recessed approximately 2.5 cm from the outer frame of the system housing. This prevented significant amount of marine aerosols to be deposited on the windows (especially as they all faced down). Pre- and postdeployment calibration of the infrared camera, as well as the data quality from the laser altimeter, confirmed that the contamination of the windows did not have measurable effects on the data, at least over the course of the short weeklong experiments. Over the course of the 4-month deployment (see below) the optical windows were cleaned every 30 days of operation. At present, the system cannot assess the cleanliness of the windows directly and continuously and is therefore not suitable for deployment without regular human intervention. The altimeter required two 6.4-cm optical-grade fused silica windows, with a third window of the same size and type for the video camera. Power was provided through two weatherproof connectors placed at the back of the housing. The first connector provided three independent 110-V lines and the second provided

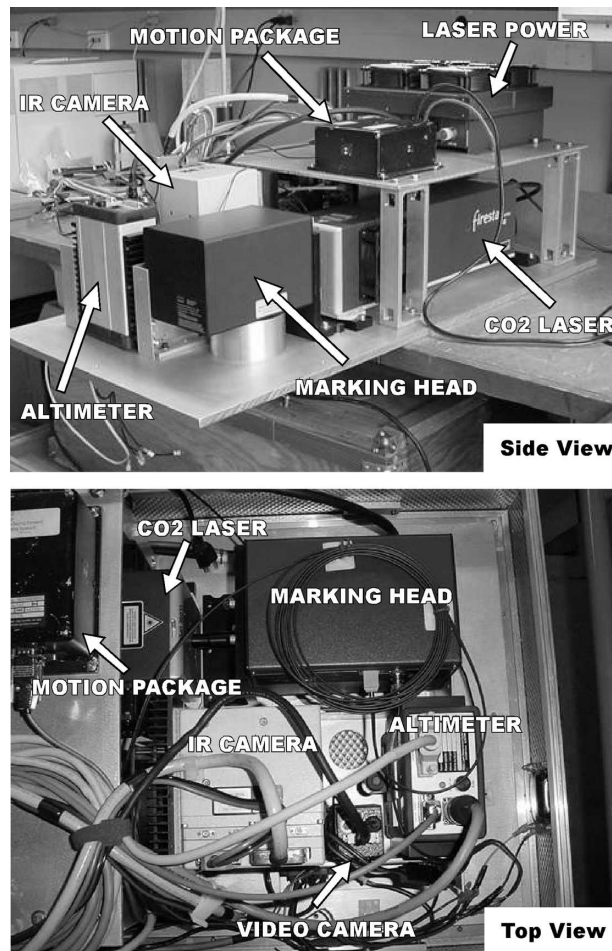


FIG. 1. Instrumentation layout for the integrated, field-deployable optical and infrared imaging and altimetry system.

a dedicated 220-V line for the CO₂ laser. Air conditioning input and exhaust were also placed at the back of the housing while four dc fans were placed inside the housing provided air circulation and cooling.

The single board computer inside the housing acquired the data from the altimeter and motion package, and served as the control computer for the CO₂ laser and marking head. Both video and infrared images were acquired with two additional dedicated PCs, which were placed outside of the housing. Data were streamed to the two PCs using two data cables with weatherproof connectors. The images were acquired directly to a striped disk set on each computer. All computers were synchronized to within 2 ms over a local network by a master PC using commercial synchronization software (Domain Time II, True Time). The master computer was in turn synchronized to GPS time.

In addition to the infrared system, we deployed one eddy covariance system to acquire supporting meteo-

rological and flux data. The eddy covariance system included a three-axis anemometer/thermometer (Campbell CSAT 3), an open-path infrared hygrometer/CO₂ sensor (Licor 7500), a relative humidity/temperature sensor (Vaisala HMP45), and a net radiometer (CNR1), all sampled at a 20-Hz rate. Turbulent fluxes of momentum, heat, and moisture were calculated over 30-min averages of the data. The sonic temperature was corrected for humidity and pressure. The rotation angles were obtained from the 30-min averages, and the latent heat flux was corrected for density variations (Webb et al. 1980).

During all experiments on board Research Platform (R/P) *FLIP*, we also deployed two fast-response, high-resolution, subsurface thermistors placed at 1.2 and 2 m from the mean water level (Branker-1040, 95 ms⁻¹ Hz sampling rate). An upward-looking waves ADCP (RDI Workhorse 600 kHz) placed at 15-m depth on the hull of R/P *FLIP* yielded directional wave spectra and significant wave height for the duration of the experiment. Finally, GPS position and R/P *FLIP* heading were sampled at a 50-Hz rate and used to correct the ADCP data for R/P *FLIP* motion.

b. Duty cycle and acquisition

The infrared camera was set to record temperature images (256 × 256 pixels) at 60 Hz, with a 2-ms integration time, yielding better than 15-mK resolution. We note here that the infrared imager was calibrated pre- and postdeployment, and temperature nonuniformity corrections were performed at sea using a uniform temperature target. The nonuniformity calibration was performed once the camera had reached its operating temperature, and it was not powered down for the remainder of the experiment. While the slope of the calibration curve (linear in the range of temperature encountered here: $r^2 = 0.99926$) is sufficiently stable to afford the repeatable relative temperature resolution quoted above, in our case the absolute temperature measurement could only be achieved to within 400 mK. This was confirmed with a comparison between the subskin temperature measurement estimated from the infrared camera and the highest subsurface thermistor measurement. Both measurements agreed within the estimated 400-mK accuracy. The absolute accuracy of the system could be improved by the use of a blackbody and frequent calibrations. Accordingly, the results and techniques presented here only rely on accurate relative temperature measurements. Calibrations and nonuniformity corrections were performed with the optical window in place to account for its effects. The video camera was set to record visible images (768 × 484 pixels) at 30 Hz. The frame grabber of the video camera

was synchronized to the frame rate of the infrared camera such that every video frame corresponds exactly to every other temperature image. In this configuration, the system acquired infrared and optical images for 20 min every hour, while the rest of the data (altimetry, motion, meteorological data) were sampled continuously for the duration of the experiments. Furthermore, the 20-min acquisition cycle alternated minute by minute between *passive infrared* data and *active infrared* data, during which time the CO₂ laser was used (see below). The laser altimeter functioned with a 12-kHz ping rate, which was then averaged down to a final 50-Hz sampling rate. The motion package was sampled at a 50-Hz rate.

All the supporting data—such as the air temperature, net radiation measurements, air humidity and atmospheric pressure, altitude, and motion data—were subsequently interpolated to a 60-Hz time base synchronized with the temperature images. The reinterpolation to a common time base is only used for “per image” type of use. For example, the altimeter and motion package data originally sampled at 50 Hz are reinterpolated to a 60-Hz time base to correct for the spatial properties (position and resolution) of each temperature image (see below). The air–sea fluxes were based on eddy covariance calculations using the 20-Hz, non-interpolated, original dataset.

c. Deployment

The measurements described here were obtained from three different field experiments. The infrared optical package, along with a standard meteorological station, was first deployed for a set of comprehensive tests from R/P *FLIP*, moored approximately 50 miles off the coast of San Diego, California (32°38.43'N, 117°57.42'W), during 21–29 July 2002. A second field experiment was then conducted from R/P *FLIP*, moored west of Tanner Bank (32°40.20'N, 119°19.46'W, 300-m depth), during 20–26 August 2003. During these experiments, the infrared optical package, the meteorological eddy covariance system, and the accompanying instrumentation described above were deployed. The instruments were deployed at the end of the port boom of R/P *FLIP* approximately 18 m from the hull at an elevation of 13 m above mean sea level (MSL). The infrared optical system was set up with the view ports clear of the end of the boom. Reflections from the boom were sometimes observed in the datasets at the lowest wind speeds (less than 2–3 m s⁻¹). These datasets were ignored in the subsequent analysis. The meteorological package was 2.5 m from the end of the boom with all instruments facing upwind with the ex-

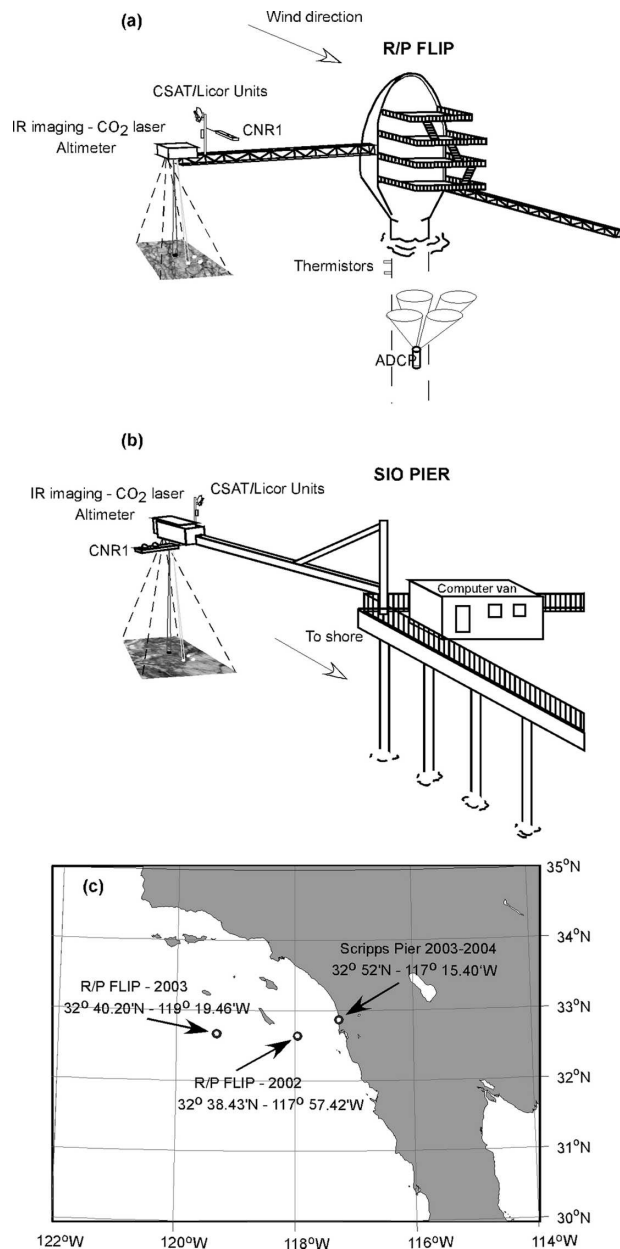


FIG. 2. (a) Instrumentation setup from R/P *FLIP*. (b) Instrumentation setup from Scripps pier. (c) Map of the deployments area. R/P *FLIP* was moored off the coast of California for two experiments in July 2002 and August 2003. The instruments were also deployed off Scripps pier during the winter 2003/04.

ception of the net radiometer, which was deployed with its axis downwind.

The complete system was also deployed from Scripps pier in a reduced acquisition mode (two 20-min records per day for the imaging systems), in the *passive infrared* mode, for approximately four months from 4 December 2003 to 6 April 2004 (Fig. 2). The same eddy covariance and infrared packages were deployed from a

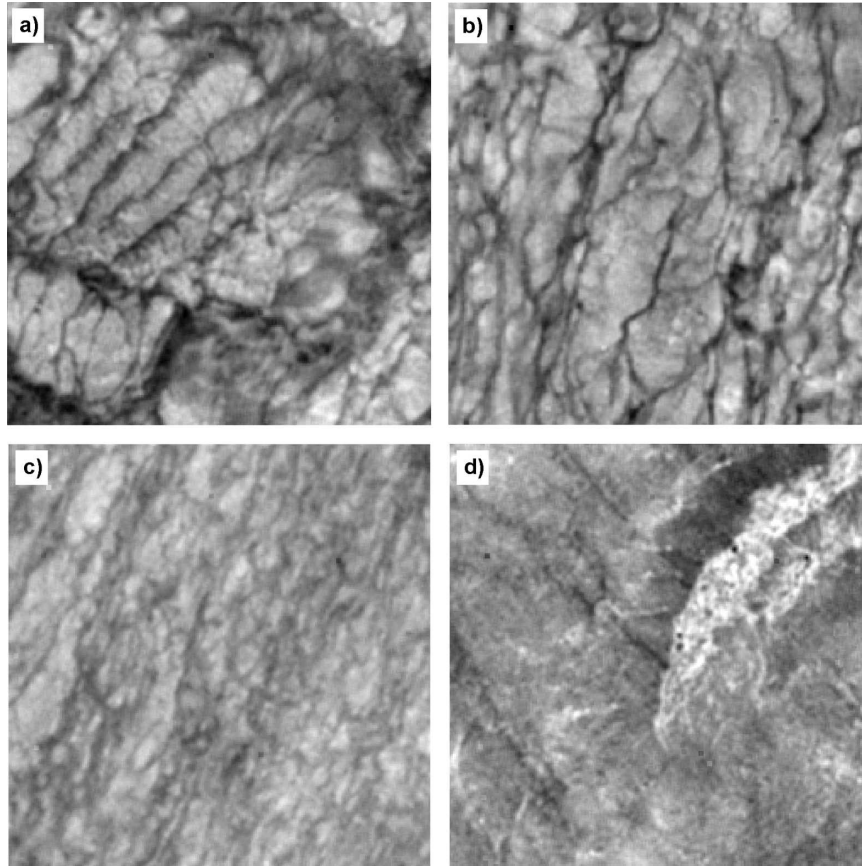


FIG. 3. Temperature images of the surface of the ocean taken from R/P *FLIP* in July 2002. The image footprints are approximately $2\text{ m} \times 2\text{ m}$. The equivalent 10-m neutral wind speed is (a) 0.1, (b) 0.9, (c) 3.8, and (d) 5.9 m s^{-1} . Image (d) also shows a breaking wave front that appears clearly as warmer temperature. The grayscale is arbitrary and represents temperature where black is cold and white is hot.

boom at the end of Scripps pier approximately 10 m out from the pier deck, at an elevation of 14 m above MSL. Subsurface temperature and supporting meteorological data were also available from the Scripps pier site in the Coastal Data Information Program (CDIP 073; more information is available online at <http://cdip.ucsd.edu>), and incident wave conditions were provided by an RDI waves ADCP seaward of the pier. Again, supporting data were acquired continuously for the entire deployment.

Representative results from all experiments are described below.

3. Results

a. Passive infrared imaging

1) SURFACE TEMPERATURE FIELDS

The passive infrared system acquired temperature images of the ocean surface at a rate of 60 Hz. In the

cases presented here, the spatial resolution was approximately 0.8 cm, but varies slightly with the altitude change due to the presence of surface waves. We have systematically corrected for this effect using the instantaneous distance from the infrared camera to the instantaneous water surface measured with the altimeter. Each temperature image therefore has its own spatial resolution, which will be used to calculate accurate displacements with both the passive [particle imaging velocimetry (PIV)-like] and the active marking methods. Both are described in detail below.

Figure 3 shows examples of ocean surface infrared images collected from R/P *FLIP* in July 2002 under various wind speed conditions. The image footprints are approximately $2\text{ m} \times 2\text{ m}$. The equivalent 10-m neutral wind speeds are 0.1 (Fig. 3a), 0.9 (Fig. 3b), 3.8 (Fig. 3c), and 5.9 m s^{-1} (Fig. 3d). The grayscale is arbitrary and represents temperature where black is cold and white is hot. Even at relatively low wind speeds (0–4 m s^{-1}) a wide range of surface temperatures and

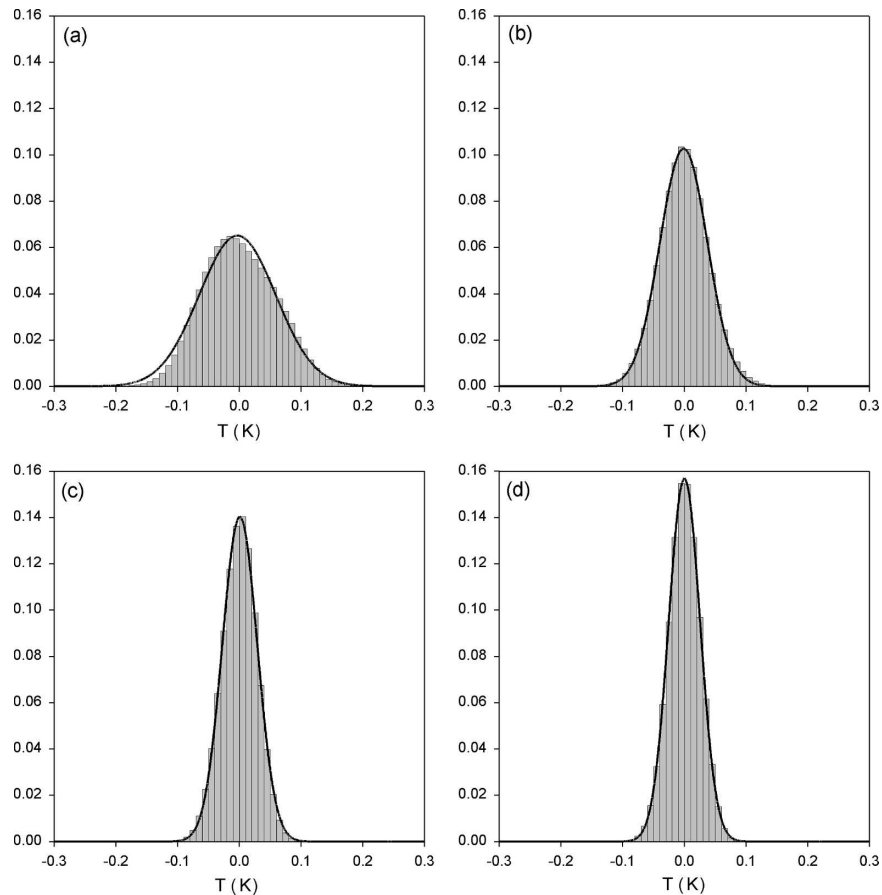


FIG. 4. Probability density functions of the surface temperature anomaly for a 10-m neutral wind speed of (a) 0.1, (b) 0.9, (c) 3.8, and (d) 5.9 m s^{-1} . The probability density functions are given in counts per increment in kelvins.

dynamical regimes are to be found. Convection patterns at the lowest wind speed are clearly visible and a transitional regime at approximately 1 m s^{-1} can be seen. As the wind speed increases, the turbulence also increases, homogenizing the temperature signal at the surface. Finally, breaking waves clearly appear at approximately $5\text{--}6 \text{ m s}^{-1}$ wind speed (Fig. 3d) as a warm patch on the image (Jessup et al. 1997). From Fig. 3, we can see that as the wind increases, the small-scale turbulence begins to dominate, resulting in a loss of contrast, or reduced variance, in the temperature images (see below). With the globally averaged wind speed (traditionally U_{10} , the wind speed at 10 m) in the range of $6\text{--}8 \text{ m s}^{-1}$, much of the time the air–sea interface is in a low-wind regime, and these images illustrate the richness of the various dynamical regimes that occur under this relatively small range of low-wind speed conditions.

Figure 4 shows the observed probability density functions (PDFs) of the surface temperature anomaly at

different wind speeds, along with the corresponding Gaussian fit to the data. To have meaningful statistics, the PDFs are constructed from 120 temperature images of the surface taken out of a minute-long set (of 3600 temperature images). Each of the 120 individual images is taken approximately every 0.5 s, the time after which we have estimated that the surface temperature field is sufficiently decorrelated for wind speeds of approximately 0.5 m s^{-1} and corresponding surface wind drift. This interval also depends on the spatial resolution and size of the footprint of the temperature image. The 0.5-s interval is further randomly varied by up to $\pm 0.2 \text{ s}$ to avoid aliasing. Statistics and PDFs are then calculated from this set of 120 temperature fields. The temperature anomaly is defined as the temperature less the mean temperature (the mean all of the data constructed from the 120 individual frames). As expected from the temperature images of Fig. 3, the range of temperatures, as measured by the variance, decreases with increasing wind speeds. Note that the observed Gaussian

form of the PDFs differs from that observed by Schimpf et al. (2004) and Haußecker et al. (2001),¹ who found that their data were adequately fitted with a function that is derived by assuming a lognormal distribution in time of the surface renewal events. The PDFs of the surface temperature anomaly become narrower, indicating that the spatial variance of the surface temperature decreases as the wind speed increases. This is simply indicating that the subsurface turbulence is more energetic, resulting in more frequent “renewals” of the surface water parcels with fluid from below and homogenization of the surface temperature. As a result, the surface residence time of water parcels is reduced and so is the time to exchange heat with the atmosphere above. Consequently, water parcels on the surface have a temperature that is much closer to that of the bulk of the fluid and the contrast in the temperature images is reduced.

The bulk skin temperature difference can be estimated from these PDFs. Indeed, the mean skin temperature is the mean of the PDFs. The bulk temperature is that of a parcel of water that just arrived at the surface and has not yet exchanged any heat with the atmosphere. Statistically, these parcels of water would therefore yield the largest temperature anomaly at the surface. In other words, the tail of the temperature PDF corresponds to the bulk temperature. This method has been successfully used by Schimpf et al. (2004) and Garbe et al. (2004), albeit with an analytical fit to the PDF.

It is probably useful to offer here a short semantic discussion. Historically, the bulk temperature has been referred to as the temperature below the skin layer, however, in many cases, the depth at which this so-called bulk temperature is given was not reported; but the measurements were presumably made a depth of at least 2–3 wave heights. However, we now know that there can be significant stratification, even in the first meter below the surface with temperature difference of order $O(1)^\circ\text{C}$. This is particularly true during the daytime when a warm diurnal layer, capped by a cool skin, leads to large stable temperature gradients and considerable confusion as to what the “bulk” temperature is. The technique outlined above leads to an estimate of the temperature difference between the skin and sub-skin. Accordingly, in the remainder of the text, we will use the term “subskin” temperature where some readers might be used to reading “bulk” temperature.

Figure 5 shows the variance of the surface tempera-

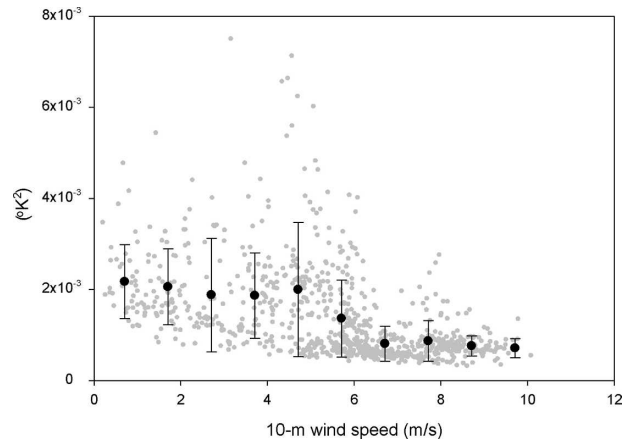


FIG. 5. Variance of the surface temperature as a function of the wind speed. The data shown represent individual minute of data and the black symbols show the bin-averaged data.

ture as a function of the wind speed. Each data point is calculated over 1 min using the same methodology as in the calculation of the probability density functions. As expected, the surface temperature variance decreases with increasing wind speed, as mixing and turbulence become more intense. Note here that if the PDFs of the surface temperature do have a Gaussian behavior, then the subskin–skin temperature difference can be directly obtained from the variance of the surface temperature. In fact, Fig. 5 is similar to plots of subskin–skin temperature differences as function of the wind speed, commonly found in the literature (Wick et al. 1996; Donlon and Robinson 1997; Donlon et al. 2002; Wick et al. 2005). Again, this is because, as suggested by Donlon et al. (1999), as the wind speed increases, molecular and convective heat transfer diminishes, and the role of shear-generated turbulent heat transfer gradually increases, with the transition from free to forced convection.

In addition to being able to measure the statistics of temperature anomalies, the infrared images allow us to obtain spatial information. For example, Fig. 6 shows two-dimensional wavenumber spectra of the surface temperature for several wind speeds. The spectra are calculated for every minute of data by averaging together 120 spectra calculated for each of the 120 temperature images used to calculate the sea surface temperature statistics as described above. The spectra shown are for wind speeds of 0.5, 3, and 8.6 m s^{-1} , and are obtained by further averaging 10 two-dimensional spectra obtained for each minute of passive acquisition period.

First, the shapes of the spectra show that the surface temperature patterns often have a preferred direction, with the “directionality,” or departure from isotropy,

¹ Upon close inspection, it appears to us that the PDF that these authors show would also be adequately represented by a Gaussian distribution.

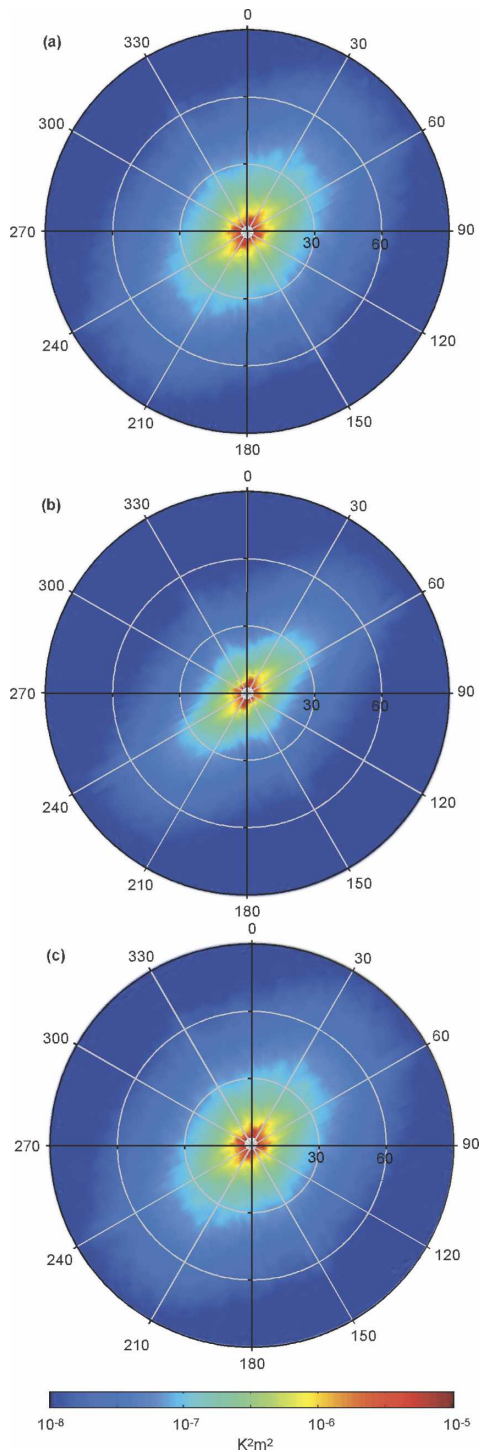


FIG. 6. Two-dimensional wavenumber spectra of the surface temperature plotted in cylindrical coordinates. The spectra shown are for 10-m wind speeds of (a) 0.5, (b) 3, and (c) 8.6 m s^{-1} and are calculated over 10 min of passive infrared acquisition.

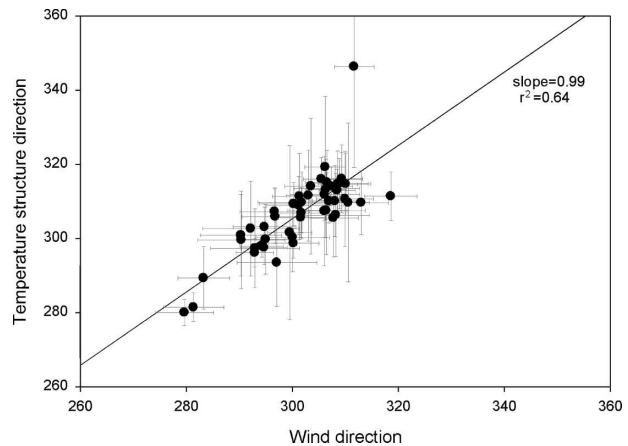


FIG. 7. Direction of the temperature structures in the images as a function of the wind direction. The fit to the data show that the temperature structures are aligned at approximately 9° to the right of the wind.

being wind speed dependent. For example, the spectrum for 3 m s^{-1} appears to be quite narrow, indicating that the temperature structures at the surface are highly organized along one direction. At lower and higher wind speeds, the spectrum is more isotropic. The anisotropy at a wind speed of approximately 3 m s^{-1} is the result of small-scale Langmuir circulations similar to those observed by Melville et al. (1998) and Veron and Melville (2001) in the same wind speed range. At other wind speeds, even when directionality is weaker, it is still possible to detect the principal direction of a spectrum, from which the direction of the temperature structures can be determined. Figure 7 shows the direction of the temperature structures in the infrared images derived from the principal axis in the two-dimensional spectra. It shows that for all wind speeds, the temperature structures are approximately aligned with the wind. In fact, a linear fit to the data provides a one-to-one correspondence between wind direction and temperature structure direction, with a correlation coefficient of $r^2 = 0.64$, and the temperature structures aligned at approximately 9° to the right of the wind.

We can further integrate the two-dimensional spectra, such as those shown in Fig. 6, and obtain omnidirectional spectra of the surface temperature. Figure 8 shows typical omnidirectional spectra of the surface temperature for different wind speeds, calculated over the 10 min of a passive acquisition period. They exhibit a -1 slope in the low wavenumber region. In general, the overall spectral levels decrease with increasing wind speed, although this is not always the case. At low wind speeds in particular, the spectral levels can vary dramatically from minute to minute. This is clear from the scatter in the data of Fig. 5. In fact, the spectral level of

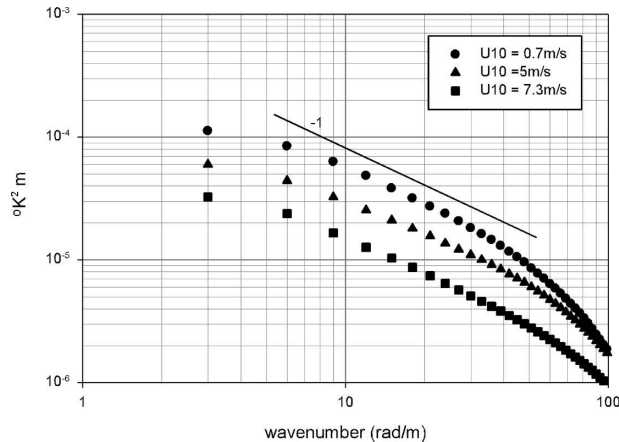


FIG. 8. Omnidirectional spectra of the surface temperature over 10 min for wind speeds of 0.7, 5.0, and 7.3 m s^{-1} .

the omnidirectional spectra can sometimes vary significantly with time (see discussion and Fig. 16).

Together, the results of Figs. 3–8 show that both time and length scales decrease with increasing wind speed.

2) SURFACE VELOCITY FIELDS

While the temperature variance diminishes with increasing wind speed, the contrast in the temperature images is, at these wind speeds, sufficient to perform analysis similar to that of PIV, on successive surface infrared images. Here we have chosen to use a normalized cross-correlation method that is similar to standard cross-correlation techniques (Raffel et al. 1998). The normalization compensates for uneven contrast in a single image or subimage. Also, warmer patterns (light) correlate in the same way as colder patterns (dark) do. In a similar fashion to that of standard PIV routines, we have performed this normalized cross-correlation analysis on subimages of the original temperature image pairs. In this case, we used 8×8 pixel subimages with 50% linear overlap and image pairs separated by 33 ms. The cross-correlation subimage then gives the average displacement between the two subimages. The average displacement and time difference between the two subimages then gives the average velocity over the subimage. In this case, this led to velocity maps at 60 Hz and containing 59×59 velocity vectors. We have tested different techniques to obtain velocity fields including cross-correlation, mean quadratic difference (MQD), and optical flow (Barron et al. 1994; Gui and Merzkirch 2000). We found that the differences were small with a slightly better performance of the cross-correlation technique in the subpixel regime (using 3-point Gaussian interpolation). The superior computing speed of the

cross-correlation technique using FFTs made this our method of choice. Cross-correlation algorithms have also been used on temperature images in the past (Garbe et al. 2004; Jessup and Phadnis 2005). In this implementation, we use a Gaussian interpolation scheme to achieve subpixel accuracy on the maximum of the correlation subimage. Our tests indicate that the rms error in pixel displacement is about 0.05 pixels, in accord with (Raffel et al. 1998). Erroneous velocities and outliers are removed from the velocity field using a dynamic mean filter (Raffel et al. 1998; Thomas et al. 2005). With the resolution of the infrared imager, this leads to errors of approximately 1 cm s^{-1} in the surface velocities. The time interval between images can be adjusted depending on the surface current and other environmental conditions. We have found here that a 33-ms time interval (every other infrared image) led, in most cases, to sufficient displacements to avoid significant errors arising from the subpixel interpolation.

In addition to measuring the velocity field at $O(1)$ -cm resolution we can also compute the mean surface current by averaging over the image. We can also infer the surface vorticity, shear strain, and divergence fields at centimeter scales, using central difference schemes applied to the velocity field (Raffel et al. 1998). Figure 9a shows an example of the velocity anomaly field calculated using the PIV algorithm on a pair of passive infrared images collected at 0509 UTC 21 July 2002, under a wind speed of 0.7 m s^{-1} . The velocity field is shown with the arrows and is overlaid on the corresponding temperature image (first of the pair). The velocity anomaly is the velocity field from which we have subtracted the mean current vector obtained from this PIV field and is shown here for easier visual comparison with the underlying temperature structures. Also shown in Fig. 9 are the vorticity and divergence fields. With these tools, the velocity field can be examined in more detail. For example, from Figs. 9b and 9c it appears that both the divergence and vorticity field show structures similar to those of the surface temperature. In particular, regions of large surface divergence correlate with regions of warmer surface temperature (not shown here). This is entirely consistent with subsurface turbulent eddies and the idea of surface renewal events (Higbie 1935; Danckwerts 1951; Haußecker et al. 1995; Garbe et al. 2004) or eddy-approach models (Atmane et al. 2004). This also appears to support recent laboratory experiments on the disruption of the surface diffusive layer in the context of gas transfer (Turney et al. 2005).

As with the temperature images, we now look at some statistical properties of the velocity, vorticity, and

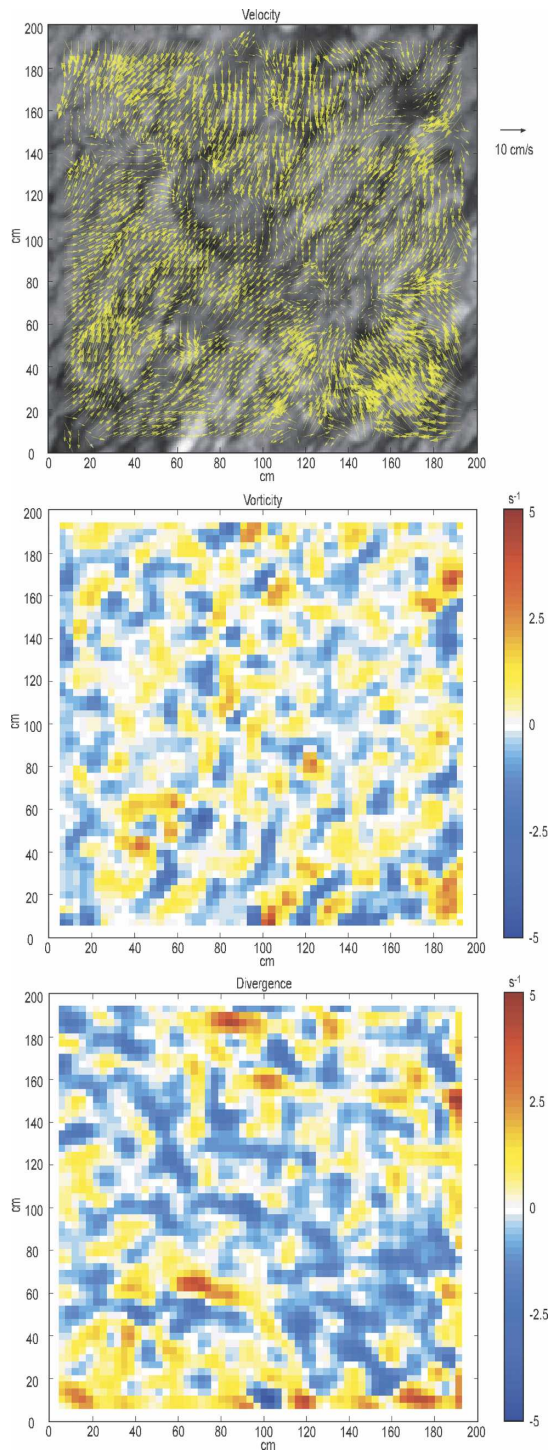


FIG. 9. Example of the velocity field (less the mean current) calculated with the PIV algorithm from surface temperature images collected at 0509 UTC 21 Jul 2002, under a wind speed of 0.7 m s^{-1} . The velocity is shown by the vector field overlaid on the first temperature image of the image pair. Also shown are the corresponding vorticity and divergence fields.

divergence fields obtained from the PIV processing of the passive infrared images. The statistics for the vorticity and divergence are collected in a similar fashion to those for the surface temperature, whereby a sub-dataset representing one *passive infrared* minute of data is constructed from vorticity and divergence images collected every 0.5 s plus a random time interval of up to $\pm 0.2 \text{ s}$. The statistics for the velocity field, however, are calculated for every one of the 120 PIV images and then averaged together. This is equivalent to filtering out spatial scales larger than the footprint of the infrared images and was done to remove the velocities associated with the wave field while retaining information about the small-scale turbulence. Figure 10 shows the PDFs of the alongwind and crosswind velocity anomaly, V_x and V_y , respectively, along with the PDFs of vorticity and divergence for a wind speed of 5.0 and 8.0 m s^{-1} . The PDFs for the velocities are not well fitted by a Gaussian distribution indicating that the field is not completely random. The departure from Gaussian is quite dramatic and occurs mostly in the tails of the distribution and especially at higher wind speed. The PDFs of the vorticity and divergence are also shown along with the corresponding best Gaussian fit to the data. It appears that the PDFs for the vorticity and divergence also depart from Gaussian, both in the tail and at the peaks of the distribution. The departure from Gaussian behavior and the implications for the surface velocity field will be discussed in a subsequent publication.

Figure 11 shows the variances of the velocity, vorticity, and divergence as a function of the wind speed. Here, the variances of the surface kinematic fields all increase with increasing wind speeds, compared with the decrease in variance for the temperature field (Fig. 5). Again, not surprisingly, this is a sign of increasing surface turbulent levels with increasing winds.

Finally, we have integrated the two-dimensional wavenumber spectra of these kinematic fields (discussed below) to obtain omnidirectional spectra. Figure 12 shows the omnidirectional spectra for the velocity magnitude, vorticity, and divergence for the same wind speeds and times as those shown in Fig. 8. As expected from the results of Fig. 11, all omnidirectional spectra show increasing spectral levels with increasing wind speeds. As for the surface temperature, spectral levels can vary significantly on short time scales. We also note here that the spectrum for the velocity shows that most of the energy is contained at the larger scales, whereas, as expected, the energy in the vorticity and divergence is contained at higher wavenumber, smaller scales.

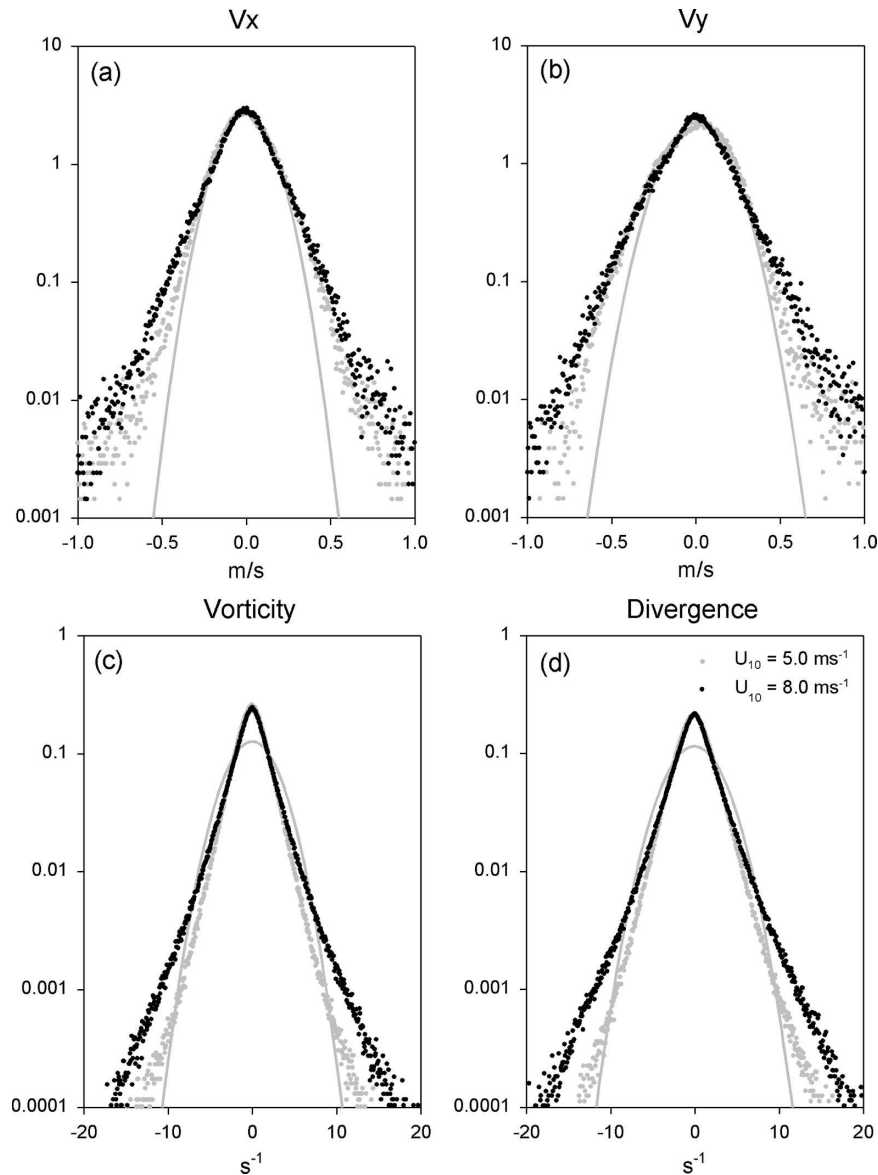


FIG. 10. Example of the probability density functions for the (a) alongwind and (b) crosswind velocity anomaly, V_x and V_y , respectively. Also shown are the PDFs for the (c) vorticity and (d) divergence. The data shown are for wind speeds of 5.0 and 8.0 m s^{-1} . The solid curves show the best Gaussian fits to the 8.0 m s^{-1} data. The PDFs shown are obtained for 1 min of data.

b. Active infrared

LAGRANGIAN HEAT MARKERS

In addition to the passive infrared temperature images of the ocean surface, we also use active infrared methods. The 60-W air-cooled CO_2 laser was used to actively mark the surface with a pattern of seven heat spots. The spots are used as passive Lagrangian markers. Each spot is approximately 3.5 cm in diameter initially. The temperature rise associated with the spot

was kept below 2 K so that buoyancy effects can be neglected. The heat markers were laid down by firing the laser for approximately 10 ms at full power. The “writing” speed and the speed of the galvanometers controlling the scanning mirrors allowed us to lay down an array of seven spots in 70 ms, corresponding to five to six temperature images. We have developed techniques that allow us to accurately follow the spots within the images. The tracking technique is based on a recognition/tracking algorithm. Initially, we identify

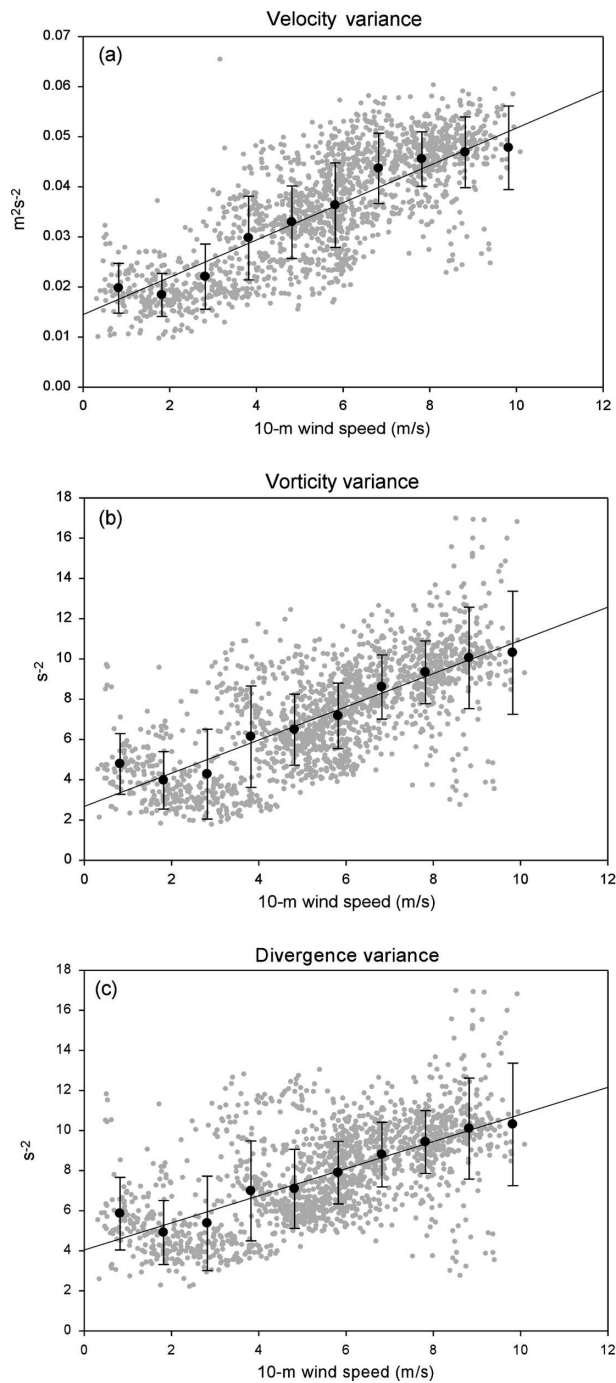


FIG. 11. Minute-by-minute variance of the surface of the (a) velocity, (b) vorticity, and (c) divergence as a function of the wind speed. The black symbols show the bin-averaged data.

which images contain the full pattern of seven spots by estimating the spatial variance in the temperature images. Indeed, the temperature contrast generated by the pattern leads to detectable enhanced temperature variance. Each spot is identified and a verification rou-

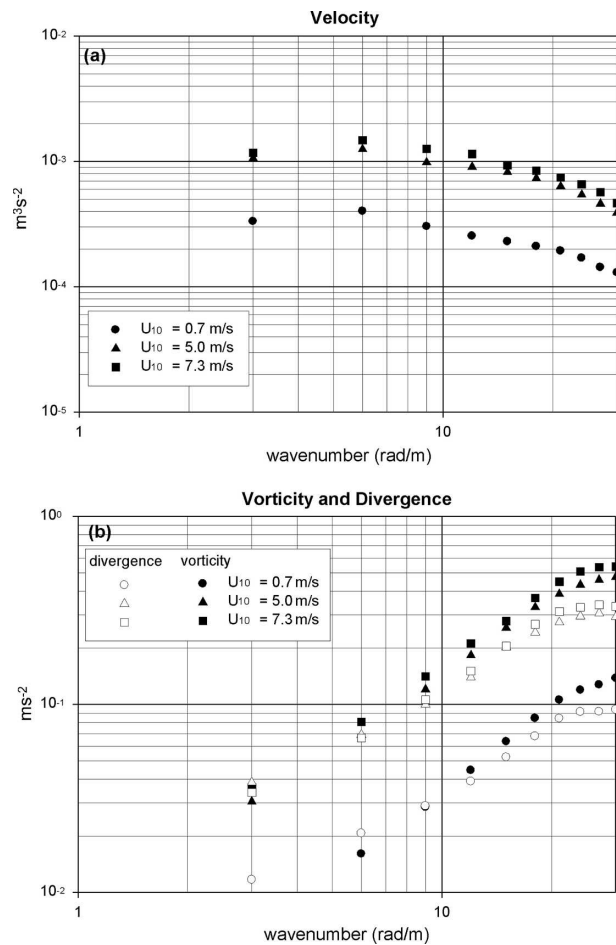


FIG. 12. (a) Omnidirectional spectra of the surface velocity over 10 min for wind speeds of 0.7, 5.0, and 7.3 m s^{-1} . (b) Omnidirectional spectra of the surface vorticity and divergence for the same data.

time based on the expected geometry of the pattern confirms that the recognition algorithm has successfully captured the full pattern. Subsequently, each spot is tracked by searching for a temperature maximum in a narrow subwindow of 10×10 pixels centered on the last known position of the spot. At first, the search algorithm is run backward in time to identify the initial marking time of individual spots within a particular temperature image. Indeed, since the complete pattern is marked during the time of acquisition of several temperature images, it is important to know exactly (within 15 ms, i.e., 60 Hz) the initial marking time for each spot. Each spot is then tracked individually until it either leaves the field of view or until the tracking algorithm fails, which is determined by the loss of continuity in the spot position. Furthermore, the position of each spot is detected with subpixel accuracy by fitting a two-dimensional Gaussian to the spot temperature pattern.

This is the best possible functional fit as the energy pattern across the laser beam is itself Gaussian. We have called this technique thermal marking velocimetry (TMV). In the present configuration, the laser marker is programmed to lay down complete patterns at a 0.5-Hz repetition rate yielding 30 patterns every minute. At very low wind speeds, spots can sometimes remain visible and detectable for more than 2 s, which means that another pattern will be marked while the previous one is still visible and being tracked. The detection/tracking algorithm handles this without any problems provided that the second pattern is laid down outside of the search region of previously marked spots. In other words, if the new pattern is laid down close to the current position of the previous one, the algorithm will discontinue tracking of the first pattern because of the loss of continuity. The tracking of the new pattern is unaffected. The displacement of the pattern itself gives an accurate measure of the (Lagrangian) average surface velocity, while the rotation, dilatation, and deformation of the pattern allows us to measure the vorticity, divergence, and shear strain fields at the surface, respectively. Figure 13a shows an example of the active infrared technique at 1402 UTC 27 July 2002, with a 1 m s^{-1} wind speed. It shows the Lagrangian heat pattern that was laid down on the surface by the CO_2 laser. The two images (separated by 665 ms) show how the pattern is displaced by the current, rotated, dilated, and sheared. The distortion of the pattern is clearly visible. Figure 13c shows the complete trajectories of the seven spots obtained by our TMV tracking routine until it stops when continuity is lost as one of the markers exits the field of view. The velocity of each spot is then calculated, as with the PIV method, by dividing the measured displacement of the laser spot over two frames by the time interval between the two frames. As with the PIV, we have used a time interval of 33 ms. Again, this time interval can be adjusted depending on the surface current and other environmental conditions. At these low wind speeds, the time interval of 33 ms led to displacements that were clearly detectable and avoided the need to rely on the subpixel interpolation. The accuracy of the subpixel interpolation in this active case is far superior to that of standard PIV techniques. This is because the interpolation is not performed on the cross-correlation subimage, but rather on the image itself. Furthermore, the power distribution across the laser beam and the heat distribution across the spot are of a Gaussian form and therefore a Gaussian fit is the best possible choice to give the position of the laser spot with subpixel accuracy. Our tests indicate that the position of a laser spot can be determined to within 0.05 of a pixel.

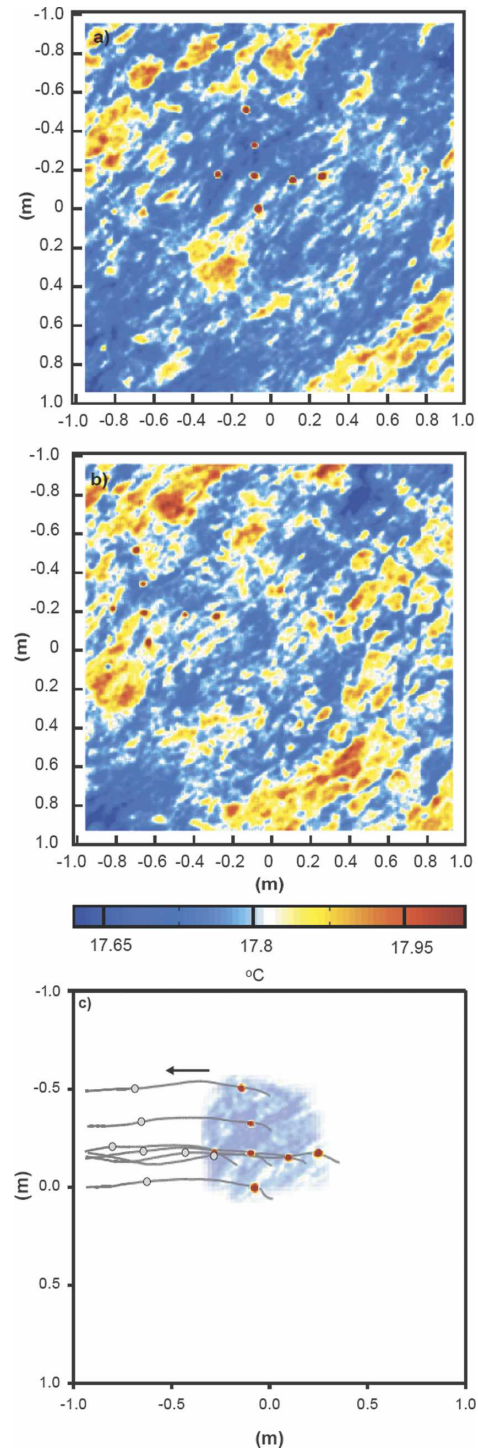


FIG. 13. Example of the Lagrangian heat pattern laid down on the surface by the CO_2 laser. (a), (b) The two images were taken at 1402 UTC 27 Jul 2002 and are separated by 665 ms. They show the pattern transported by the mean current and distorted. (c) The complete trajectories of the spots obtained by the TMV tracking routine.

We next compare the velocity obtained with the TMV method on individual spots with the velocity obtained with the PIV routine. Figure 14 shows a time series of the TMV velocity for a single spot of the pattern for 1 min of data under a wind speed of 2.7 m s^{-1} . Here we have compared the (Lagrangian) velocity of the laser spot with the velocity from the PIV velocity field and interpolated to the laser spot position. Also shown is the average velocity (over the entire PIV velocity field) for that particular minute of data.² The time series of the velocity of the laser spot from the TMV method (black dots) agrees very well with the time series of the PIV velocity interpolated at the spot position (black line). Figure 14b shows the velocity from the TMV plotted against the velocity from the PIV for the same minute of data as shown in Fig. 14a. The agreement is very good and the fit to the data gives a slope of 0.99 and a correlation (r^2) of 0.98. While the actual TMV algorithm by which laser dots are identified and tracked within the temperature image is quite complicated, the principle of the method is very simple. The agreement between the passive and active methods allows us to conclude that PIV-type analysis on passive infrared surface temperature yields good surface velocity fields. At high wind speeds, however, the passive technique will break down when temperature structures disappear, rendering the cross-correlation routines noisy. In that case, the active technique is the appropriate method.

The vorticity, shear strain, and divergence are next obtained from the rotation, deformation, and dilatation of the pattern. The pattern is divided into 29 triplets of points, all forming triangles (the technique fails if the three spots are aligned). Individual triplets yield vorticity and divergence as follows. For each triplet of spots, the velocities of the spots at the ends of each side of the included triangle are interpolated into tangential, U_{\parallel} , and orthogonal, U_{\perp} , velocity components at the center of the respective side. The vorticity and divergence given by each triplet of spots is then calculated as an area average and obtained from the line integrals along the closed triangle of U_{\parallel} (along) and U_{\perp} (across):

$$\omega = \frac{1}{A} \oint U_{\parallel} dl, \quad (1)$$

$$D = \frac{1}{A} \oint U_{\perp} dl, \quad (2)$$

where A is the area of the triangle formed by the triplet, and in this case taken as the averaged area of the tri-

² This minute of data was chosen randomly; similar agreement is obtained for all other data.

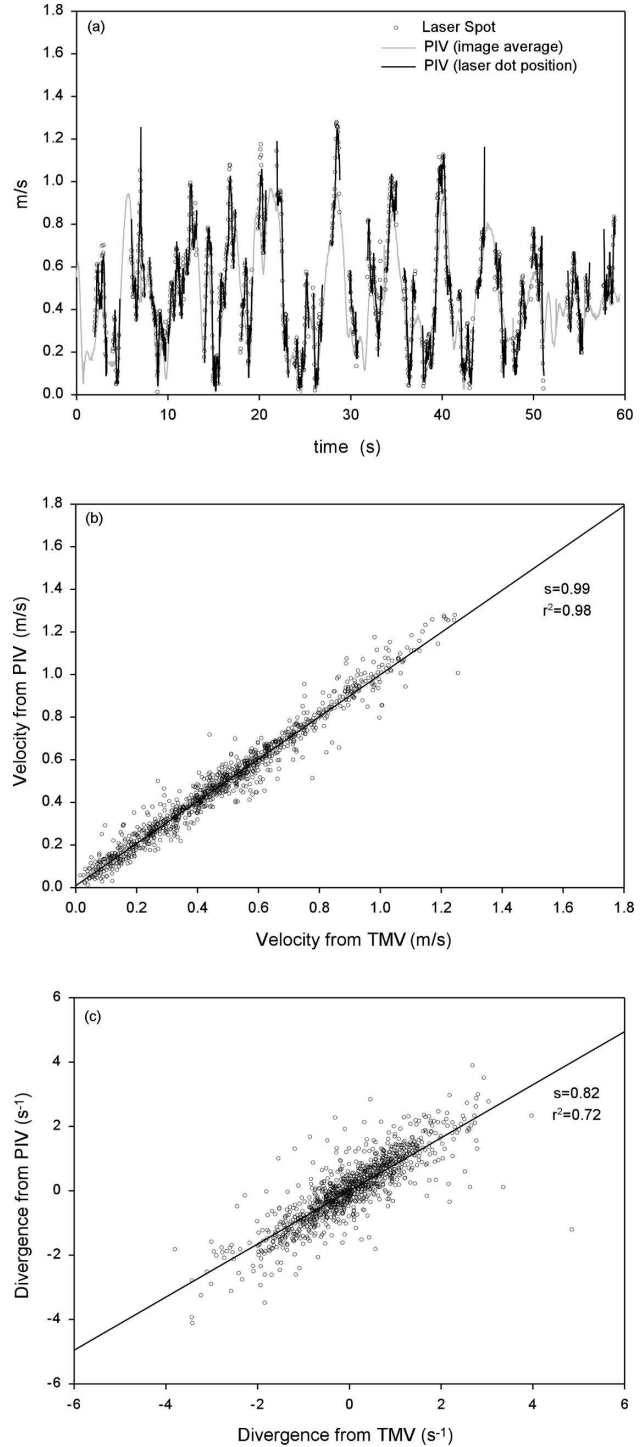


FIG. 14. (a) Time series of the velocity of a single marker over 1 min (dots) obtained from the TMV algorithm, along with the time series of the velocity obtained from the PIV and interpolated to the marker position. (b) The velocity from the TMV plotted against the velocity from the PIV. The solid line is the linear fit to the data. (c) The divergence from the TMV plotted against the divergence from the PIV along with the linear fit to the data.

angles in the two consecutive frames. Obviously, as with finite-difference-type methods such as PIV, the time interval needs to be small enough for the finite difference to represent a first-order derivative. Figure 14c shows the divergence of one triplet of laser spots as a function of the divergence obtained from the PIV data over the same minute of data as shown in Fig. 14a. For comparison, the divergence obtained from PIV is obtained also from Eq. (2), but using the velocity field calculated with the PIV algorithm. Agreement between the active and passive divergence is not as good as that obtained with the velocity as should be expected when dealing with first-order derivatives of the data. Nonetheless, the agreement is quite remarkable, yielding a linear fit with correlation r^2 of 0.72 and a slope of 0.82. We have determined that the slope lower than one is due to the error on the subpixel interpolation for the PIV data. Removing the divergence data calculated from PIV velocities of less than one pixel (per pair of frames) leads to correlation r^2 of 0.82 and a slope of 0.86.

In addition to providing precise measurements of the surface kinematics, at least at the scale of the marker array, the temporal thermal signature of the active marker can be related to the heat flux through the surface. The exponential decay rate λ of the temperature spots gives a measure of the surface heat transfer velocity k_H . This technique is commonly referred to as the active controlled flux technique (ACFT; Haußecker et al. 1995; Zappa et al. 2001; Garbe et al. 2004; Asher et al. 2004; Atmane et al. 2004). It uses a surface renewal model that leads to the estimate of k_H based on the time scale obtained by the spot decay rates $k_H = \sqrt{k\lambda}$, where k is the diffusivity of heat. The net heat flux at the surface can be estimated with

$$Q_{\text{net}} = k_H \rho C_p \Delta T, \quad (3)$$

where ρ and C_p are the density and the specific heat of water, respectively, and ΔT is the temperature difference across the thermal diffusive layer, that is, the temperature difference between the subskin fluid and the skin.

To estimate k_H , we need to estimate the time scale associated with the exponential decay rate of the normalized temperature of the heat markers:

$$T_n = \frac{T_m - T_s}{T_{m0} - T_s}, \quad (4)$$

where T_m is the spot temperature, T_s the average temperature of the surface in the neighborhood of the individual spots, and T_{m0} is the temperature of a spot at $t = 0$, the time at which it is initially detected. For this reason, and since the temperature decay rate is expo-

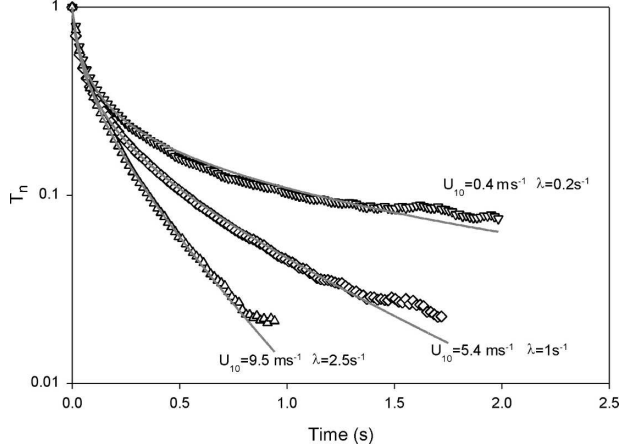


FIG. 15. Example of the temperature as a function of time of the heat markers. Each decay curve is averaged over the seven spot pattern and then further averaged over 1 min (30 patterns). The solid curve shows the theoretical fit (Haußecker et al. 1995).

ponential, we need to determine the initial marking time of each spot individually rather than the initial marking time of the full pattern. This is achieved by the algorithm that tracks the position of each marker. For the purpose of averaging together the decay curve of the pattern, each of the seven spots is assigned its own relative time, which starts at the initial detection of the spot in question. We then average all the normalized temperature curves for the pattern and obtain a single estimate of the decay rate λ for the pattern. This then gives us 30 estimates of λ per minute, which are then averaged together. We found that this was not significantly different from averaging all decay curves for a single minute and obtaining a single λ for that particular minute. This indicates that an average of seven temperature decay curves is sufficient to obtain a good estimate of λ . In the present algorithm, since the exponential fit is more computationally expensive than making averages, we choose to calculate an average temperature decay curve over an entire minute and then estimate a single λ . This yields an estimate of the surface heat transfer velocity for every *active infrared* minute. Figure 15 shows the normalized temperature T_n of the seven spots in the pattern averaged over 1 min of data and for different wind speeds. The solid curves show the theoretical decay rate of the temperature; the agreement is very good. We find that a typical error on the spot temperature decay rate is of $O(0.01) s^{-1}$ yielding an error in the heat transfer velocity k_H of approximately $O(1)\%$. One of the interesting aspects of this method is that it permits us to measure concurrently the kinematics of the surface using the TMV, as well as an estimate of the surface heat flux using the ACFT technique.

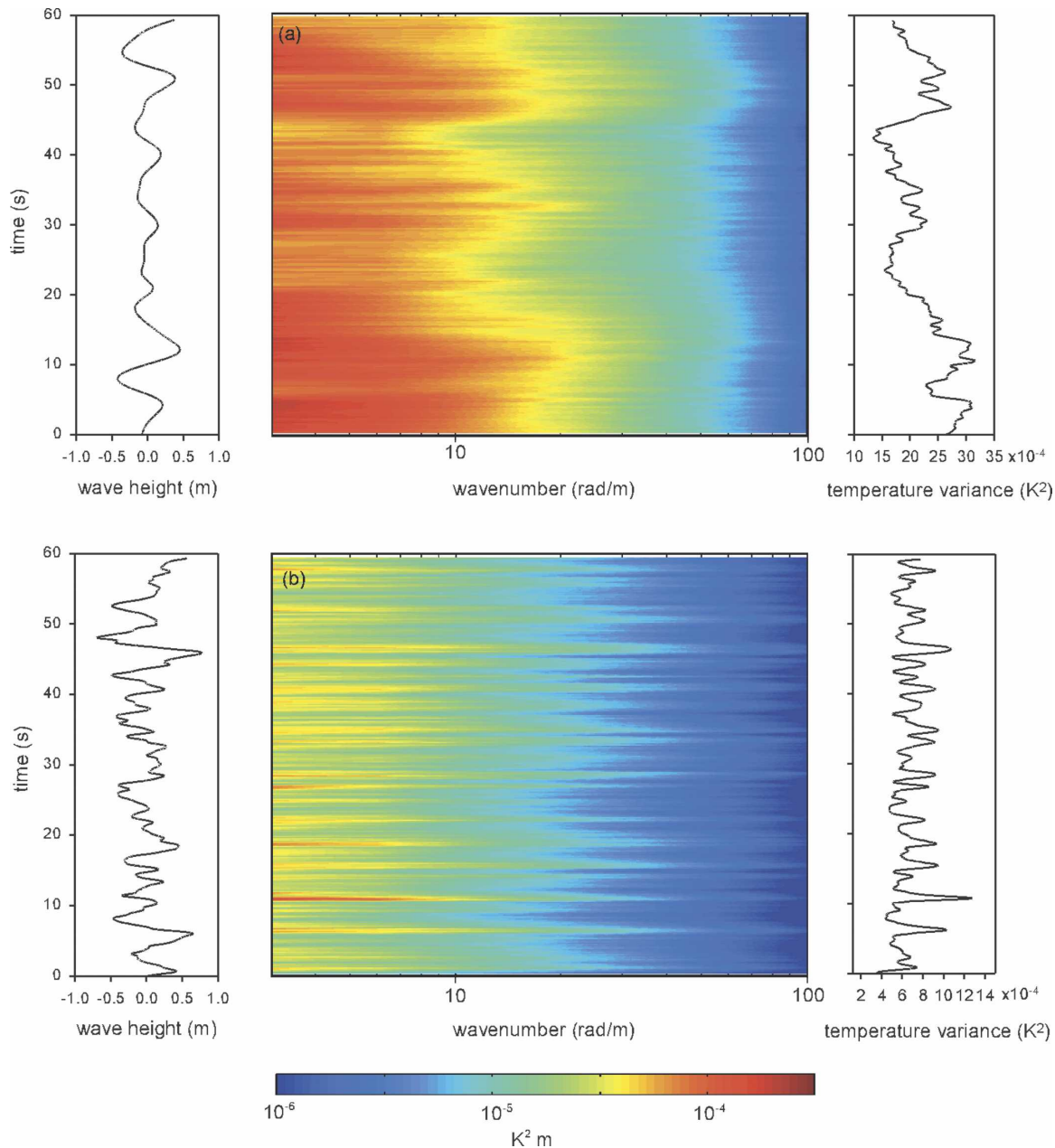


FIG. 16. Omnidirectional spectragrams of the surface temperature over 1 min for wind speeds of (a) 0.7 and (b) 7.3 m s⁻¹. Also shown are the surface wave elevation and temperature variance over the same time periods. The correlation coefficients between the surface elevation and temperature variance time series are 0.27 and 0.29 for the 0.7 and 7.3 m s⁻¹ wind speeds, respectively.

4. Discussion

This paper has been specifically aimed at showing the use and limitations of passive and active infrared techniques for studying multiple processes at the surface of the ocean. In particular, we have seen that infrared images of the ocean surface can be collected and processed to give simultaneous measurements of the SST, air-sea heat fluxes, and surface velocity fields including

mean current and wave orbital motion, and turbulence. There are several aspects of the interaction between the temperature, surface displacement, and surface velocity fields that will be discussed in subsequent publications. However, to illustrate the complexity and richness of the problem at hand, we show several examples of such correlations.

Figure 16 shows two omnidirectional spectragrams of the surface temperature for wind speeds of 0.7 and

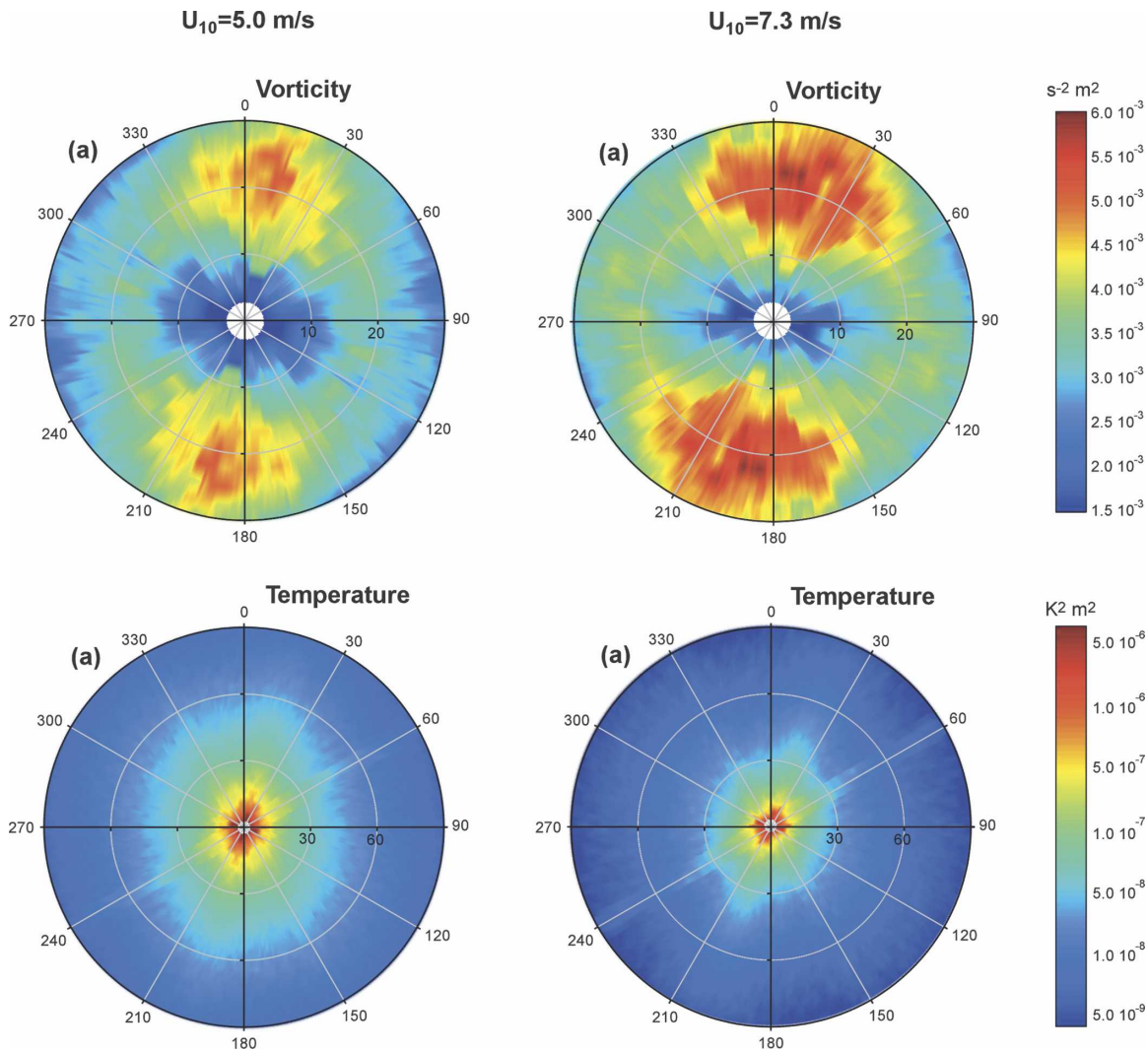


FIG. 17. Two-dimensional wavenumber spectra of the vorticity and surface temperature for wind speeds of 5.0 and 7.3 m s^{-1} .

7.3 m s^{-1} over 1 min. The spectragrams show that there are significant modulations of the spectral levels. Along with the spectragrams, we show the surface wave elevation and the variance within the infrared images. While it is clear that the modulation of the omnidirectional surface temperature spectra occurs on a time scale comparable with the surface wave period, a one-to-one correspondence is more difficult to establish visually. Yet it is clear that the spectra, and therefore the surface temperature patterns, are modulated by the surface wave field. The correlation coefficients between the surface elevation and temperature variance are 0.27 and 0.29 for the 0.7 and 7.3 m s^{-1} wind speeds, respectively.

Of particular value in the measurements shown here is the ability to simultaneously measure several variables. A particular example is provided by the two-

dimensional spectra of the vorticity and surface temperature. Figure 17 shows the two-dimensional wavenumber spectra for the vorticity calculated from the PIV images and that for the surface temperature (see Fig. 6) during the same minute of data. The data shown were collected under wind speeds of 5.0 and 7.3 m s^{-1} . The spectrum of the vorticity is approximately aligned with that of the temperature. This is a result of the coupling between surface temperature and velocity. We know from previous work (Veron and Melville 2001) that small-scale Langmuir circulations and coherent turbulence (streaks) are present at these scales over this range of wind speeds. Even if instantaneous realization of the surface temperature and velocity do not exhibit such structures, a time average will reveal their presence. Also, colder streaks in the temperature images correspond to water parcels that have been organized

by the underlying Langmuir cells and have collected in windrows at the surface. These water parcels have been in contact with the air the longest and therefore have had the time to exchange significant heat, hence the colder temperature. In addition, these parcels of water also have been exposed to the wind stress the longest, and therefore the “cold” surface temperature streaks also correspond to surface “jets” where within the streaks the surface velocity is larger than that of the surrounding fluid. This is illustrated in Leibovich (1983). As a consequence of this, there are two horizontal shear layers on each side of the temperature streaks. These lead to streaks, parallel to the temperature structures, where vertical vorticity is enhanced. In turn, this is the positive feedback between the surface jets, vertical vorticity, and the shearing of the vertical vortex lines by the Stokes drift that lead to the formation of Langmuir circulations (Craik 1977; Leibovich 1977). This result is supported by the patterns in Fig. 9, where the vorticity field is aligned with the surface temperature.

The results shown on Figs. 16 and 17 clearly illustrate the complexity of the turbulence within the viscous and thermal surface sublayers and the consequent interaction between surface temperature and kinematic fields. These data illustrate the need to study both these surface processes with an integrated approach. Such studies are made possible by the instrumentation presented in this paper.

5. Conclusions

We have successfully developed, tested, and deployed an integrated optical and infrared imaging and altimetry system for studies of the air–sea interface and air–sea interaction. The system is capable of continuously acquiring 20 min of video and temperature images of the ocean surface. During the 20 min, a user-selectable fraction of time can be designated as “active,” which means that a CO₂ laser will be used to lay down heat markers that can be detected by the infrared imager and therefore used as Lagrangian markers. The system also continuously acquires GPS position and altimetry (wave height). Surface temperature images have been used to give statistical descriptions of the temperature field. In particular, by acquiring a large number of images, significant statistics can be constructed and the subskin–skin temperature can be inferred from the probability density function of the surface temperature anomaly. The surface temperature images also permit PIV measurements of the surface velocity field and its first derivatives, including vorticity and divergence. This leads to the possibility of studying

the coupling of the surface temperature and velocity fields at the resolution of the imager. We have also shown that active marking of the surface also yields accurate Lagrangian velocities from which surface kinematic properties can be readily calculated. The active technique, which we call thermal marking velocimetry (TMV), has multiple advantages. It does not rely on the ambient temperature field and therefore is expected to work under higher wind speeds where the passive velocimetry technique would fail for lack of temperature contrast. It also yields an estimate of the surface renewal time scale obtained by the observed decay rate of the heat markers.

Together, the combination of instruments and techniques presented here provide the opportunity to study, at scales of order centimeters and larger, the relationships between the surface temperature and velocity fields, their statistics, spectra, and related kinematic descriptions. Along with the controlled flux technique, these techniques can provide much improved measurements of the relationship between air–sea heat flux and surface turbulence. This will be described in subsequent publications.

Acknowledgments. We thank Peter Matusov for his help in the design, construction, testing, and deployment of the original instrumentation. We thank Bill Gaines, and the captain and crew of the R/P *FLIP* for all their help in the field experiments. We thank John Hildebrand and Gerald D’Spain for sharing space and facilities on R/P *FLIP*. Charly Coughran and the staff of the SIO Hydrodynamics Laboratory assisted in deploying equipment off Scripps pier. We thank the staff of the SIO Marine Development Shop for the fabrication of the custom equipment. This research was supported by an NSF Grant (OCE 01-18449) to WKM and FV and an ONR (Physical Oceanography) grant to WKM.

REFERENCES

- Agrawal, Y., E. Terray, M. Donelan, P. Hwang, A. J. Williams III, W. M. Drennan, K. K. Kahma, and S. A. Kitaigorodskii, 1992: Enhanced dissipation of kinetic energy beneath surface waves. *Nature*, **359**, 219–220.
- Anis, A., and J. N. Moum, 1995: Surface wave–turbulence interactions, scaling $\varepsilon(z)$ near the sea surface. *J. Phys. Oceanogr.*, **25**, 2025–2045.
- Asher, W. E., A. T. Jessup, and M. A. Atmane, 2004: Oceanic application of the active controlled flux technique for measuring air–sea transfer velocities of heat and gases. *J. Geophys. Res.*, **109**, C08S12, doi:10.1029/2003JC001862.
- Atmane, M. A., W. E. Asher, and A. T. Jessup, 2004: On the use of the active infrared technique to infer heat and gas transfer

- velocities at the air-water free surface. *J. Geophys. Res.*, **109**, C08S14, doi:10.1029/2003JC001805.
- Barron, J. L., D. J. Fleet, and S. Beauchemin, 1994: Performance of optical flow techniques. *Int. J. Comput. Vision*, **12**, 43–77.
- Castro, S. L., G. A. Wick, and W. J. Emery, 2003: Further refinements to models for the bulk-skin sea surface temperature difference. *J. Geophys. Res.*, **108**, 3377, doi:10.1029/2002JC001641.
- Craik, A. D. D., 1977: The generation of Langmuir circulations by an instability mechanism. *J. Fluid Mech.*, **81**, 209–223.
- Danckwerts, P. V., 1951: Significance of liquid-film coefficients in gas absorption. *Ind. Eng. Chem.*, **43**, 1460–1467.
- Donlon, C. J., and I. S. Robinson, 1997: Observations of the oceanic thermal skin in the Atlantic Ocean. *J. Geophys. Res.*, **102**, 18 585–18 606.
- , W. Eifler, and T. J. Nightingale, 1999: The thermal skin temperature of the ocean at high wind speed. *Proc. IGARSS '99 Geoscience and Remote Sensing Symp.*, Hamburg, Germany, IEEE, 8–10.
- , P. Minnett, C. Gentemann, T. J. Nightingale, I. J. Barton, B. Ward, and J. Murray, 2002: Toward operational validation of satellite sea surface skin temperature measurements for climate research. *J. Climate*, **15**, 353–369.
- Ewing, G., and E. D. McAlister, 1960: On the thermal boundary layer of the ocean. *Science*, **131**, 1374–1376.
- Fairall, C. W., E. F. Bradley, D. P. Rogers, J. B. Edson, and G. S. Young, 1996: Bulk parameterization of air-sea fluxes for Tropical Ocean-Global Atmosphere Coupled-Ocean Atmosphere Response Experiment. *J. Geophys. Res.*, **101**, 3747–3764.
- Garbe, C. S., U. Schimpf, and B. Jähne, 2004: A surface renewal model to analyze infrared image sequences of the ocean surface for the study of air-sea heat and gas exchange. *J. Geophys. Res.*, **109**, C08S15, doi:10.1029/2003JC001802.
- Gui, L., and W. Merzkirch, 2000: A comparative study of the MQD method and several correlation-based PIV evaluation algorithms. *Exp. Fluids*, **28**, 36–44.
- Hasse, L., 1990: On the mechanism of gas exchange at the air-sea interface. *Tellus*, **42B**, 250–253.
- Haußecker, H., S. Reinelt, and B. Jähne, 1995: Heat as a proxy tracer for gas exchange measurements in the field: Principles and technical realization. *Proc. Third Int. Symp. on Air-Water Gas Transfer*, Heidelberg, Germany, Image Processing, 405–413.
- , U. Schimpf, C. S. Garbe, and B. Jähne, 2001: Physics from IR image sequences: Quantitative analysis of transport models and parameters of air-sea gas transfer. *Gas Transfer at Water Surfaces*, *Geophys. Monogr.*, Vol. 127, Amer. Geophys. Union, 103–108.
- Higbie, R., 1935: The rate of absorption of a pure gas into a still liquid during short periods of exposure. *Trans. Amer. Inst. Chem. Eng.*, **31**, 365–389.
- Hill, R. W., 1972: Laboratory measurement of heat transfer and thermal structure near an air-water interface. *J. Phys. Oceanogr.*, **2**, 190–198.
- Jähne, B., and H. Haußecker, 1998: Air-water gas exchange. *Annu. Rev. Fluid Mech.*, **30**, 443–468.
- , K. O. Munnich, R. Bosinger, A. Dutzi, W. Huber, and W. Libner, 1987: On the parameters influencing air-water gas exchange. *J. Geophys. Res.*, **92**, 1937–1949.
- Jessup, A. T., and K. R. Phadnis, 2005: Measurement of the geometric and kinematic properties of microscale breaking waves from infrared imagery using a PIV algorithm. *Meas. Sci. Technol.*, **16**, 1961–1969.
- , C. J. Zappa, and J. H. Yeh, 1997a: Defining and quantifying microscale breaking with infrared imagery. *J. Geophys. Res.*, **102**, 23 145–23 153.
- , —, M. R. Loewen, and V. Hesany, 1997b: Infrared remote sensing of breaking waves. *Nature*, **385**, 52–55.
- Leibovich, S., 1977: On the evolution of the system of wind drift current and Langmuir circulations in the ocean. Part 1: Theory and average current. *J. Fluid Mech.*, **79**, 715–743.
- , 1983: The form and dynamics of Langmuir circulations. *Annu. Rev. Fluid Mech.*, **15**, 391–427.
- McAlister, E. D., 1964: Infrared-optical techniques applied to oceanography I. Measurement of total heat flow from the sea surface. *Appl. Opt.*, **5**, 609–612.
- , and W. A. McLeish, 1970: Radiometric system for airborne measurement of the total heat flow from the sea. *Appl. Opt.*, **9**, 2607–2705.
- Melville, W. K., 1994: Energy dissipation by breaking waves. *J. Phys. Oceanogr.*, **24**, 2041–2049.
- , 1996: The role of surface-wave breaking in air-sea interaction. *Annu. Rev. Fluid Mech.*, **28**, 279–321.
- , R. Shear, and F. Veron, 1998: Laboratory measurements of the generation and evolution of Langmuir circulations. *J. Fluid Mech.*, **364**, 31–58.
- Raffel, M., C. E. Willert, and J. Kompenhans, 1998: *Particle Image Velocimetry: A Practical Guide*. Springer-Verlag, 253 pp.
- Saunders, P. M., 1967: The temperature at the ocean-air interface. *J. Atmos. Sci.*, **24**, 269–273.
- Schimpf, U., C. Garbe, and B. Jähne, 2004: Investigation of transport processes across the sea surface microlayer by infrared imagery. *J. Geophys. Res.*, **109**, C08S13, doi:10.1029/2003JC001803.
- Schlüssel, P., W. J. Emery, H. Grassl, and T. Mammen, 1990: On the bulk-skin temperature difference and its impact on satellite remote sensing of the sea surface temperature. *J. Geophys. Res.*, **95**, 13 341–13 356.
- Soloviev, A. V., and P. Schlüssel, 1994: Parameterization of the cool skin of the ocean and of the air-ocean gas transfer on the basis of modeling surface renewal. *J. Phys. Oceanogr.*, **24**, 1339–1346.
- Terray, E., M. Donelan, Y. Agrawal, W. Drennan, K. Kahma, A. Williams, P. Hwang, and S. Kitaigorodskii, 1996: Estimates of kinetic energy dissipation under breaking waves. *J. Phys. Oceanogr.*, **26**, 792–807.
- Thomas, M., S. Misra, C. Kambhmettu, and J. T. Kirby, 2005: A robust motion estimation algorithm for PIV. *Meas. Sci. Technol.*, **16**, 865–877.
- Thorpe, S. A., 1993: Energy loss by breaking waves. *J. Phys. Oceanogr.*, **23**, 2498–2502.
- Turney, D. E., W. C. Smith, and S. Banerjee, 2005: A measure of near-surface fluid motions that predicts air-water gas transfer in a wide range of conditions. *Geophys. Res. Lett.*, **32**, L04607, doi:10.1029/2004GL021671.
- Veron, F., and W. K. Melville, 1999a: Pulse-to-pulse coherent Doppler measurements of waves and turbulence. *J. Atmos. Oceanic Technol.*, **16**, 1580–1597.
- , and —, 1999b: Laboratory studies of mixing and Langmuir circulations. *Proc. Fourth Int. Symp. on the Wind-Driven Air-Sea Interface*, Sydney, Australia, Australian Defense Force Academy, 265–272.

- , and —, 2001: Experiments on the stability and transition of wind-driven water surfaces. *J. Fluid Mech.*, **446**, 25–65.
- Webb, E. K., G. I. Pearman, and R. Leuning, 1980: Measurements for density effects due to heat and water vapor transfer. *Quart. J. Roy. Meteor. Soc.*, **106**, 85–106.
- Wick, G. A., W. J. Emery, and P. A. Schlüssel, 1992: A comprehensive comparison between satellite-measured skin and multichannel sea surface temperature. *J. Geophys. Res.*, **97**, 5569–5595.
- , —, L. H. Kantha, and P. Schlüssel, 1996: The behavior of the bulk–skin sea surface temperature difference under varying wind speed and heat flux. *J. Phys. Oceanogr.*, **26**, 1969–1988.
- , J. C. Ohlmann, C. W. Fairall, and A. T. Jessup, 2005: Improved oceanic cool-skin corrections using a refined solar penetration model. *J. Phys. Oceanogr.*, **35**, 1986–1996.
- Zappa, C. J., and A. T. Jessup, 2005: High-resolution airborne infrared measurements of ocean skin temperature. *IEEE Trans. Geosci. Remote Sens. Lett.*, **2**, 146–150.
- , W. E. Asher, and A. T. Jessup, 2001: Microscale wave breaking and air-water gas transfer. *J. Geophys. Res.*, **106**, 9385–9391.